

Article

# Free Vibration Analysis of a Reconfigurable Modular Morphing Wing

Faisal Mahmood, Seyed M. Hashemi  and Hekmat Alighanbari \*

Department of Aerospace Engineering, Toronto Metropolitan University, Toronto, ON M5B 2K3, Canada

\* Correspondence: halighan@ryerson.ca; Tel.: +1-416-979-5000-X-557736

**Abstract:** Aircraft experience various phases during each flight. Optimal performance, without compromise, during various phases can be achieved through adaptability in the wing design. Morphing wing design encompasses most, if not all, the flight conditions variations, and can respond interactively. In the present work, the dynamic characteristics of a reconfigurable modular morphing wing of two topological architectures, developed in-house by a research group at Toronto Metropolitan University (formerly Ryerson University), were investigated. This modular morphing wing, developed based on the idea of a parallel robot, consists of a number of structural elements connected to each other and to the wing ribs through eye-bolt joints. Euler–Bernoulli and Timoshenko bending beam theories, in conjunction with Finite Element Analysis, were exploited. Free vibration of unmorphed (Original) and morphed configurations subjected to spanwise extensions were studied. The results of systems' free vibration analyses were validated against those obtained from Ansys and Dynamic Stiffness Matrix (DSM) method. The effect of various spanwise extensions, as well as topology on system's natural frequencies, was also studied and reported on.

**Keywords:** numerical modal analysis; morphing wing; finite element analysis; dynamic stiffness matrix; spherical joints; Timoshenko beam



**Citation:** Mahmood, F.; Hashemi, S.M.; Alighanbari, H. Free Vibration Analysis of a Reconfigurable Modular Morphing Wing. *Aerospace* **2022**, *9*, 532. <https://doi.org/10.3390/aerospace9100532>

Academic Editor: Xiaowei Chen

Received: 1 July 2022

Accepted: 30 August 2022

Published: 21 September 2022

**Publisher's Note:** MDPI stays neutral with regard to jurisdictional claims in published maps and institutional affiliations.



**Copyright:** © 2022 by the authors. Licensee MDPI, Basel, Switzerland. This article is an open access article distributed under the terms and conditions of the Creative Commons Attribution (CC BY) license (<https://creativecommons.org/licenses/by/4.0/>).

## 1. Introduction

In the current evolving design era of seeking high performance along with economical design intent, adaptability in response to the changing environment is deemed a highly desired prospect. This concept of adaptability has been successfully implemented in a number of industries ranging from daily life furniture to transportation. The aerospace industry has successfully responded to this global trend as well. Fixed wing aircraft have been considered the culmination of the human dream of flying. However, evolutionary technological breakthroughs with the passage of time and current trends in marketing and competitive products have influenced the researchers to investigate novel ways to design and develop aircraft to accommodate adaptability during different flight phases. Exposed to various flight phases and gust conditions, logical evolution of aircraft design leads to what is generally termed as morphing wings. Changing wings in terms of sizes or orientation is a giant step towards the current adaptability trend. Although still at the rudimentary stage, morphing wings generally offer adaptability, but not for all varying situations simultaneously, namely spanwise, dihedral and sweep variations. It is widely accepted and agreed that hinged devices, such as flaps, ailerons and slats, are not considered morphing devices.

It has been shown that, with the application of morphing wings, several advantages can be achieved including high lift-to-drag ratio, manoeuvrability and flight envelop expansion [1,2]. The idea of morphing wing has already been implemented in some military aircraft including Grumman F14 Tomcat, Bell Boeing V-22 Osprey, and BAE-Systems Concorde, equipped with variable sweep-wing, colloquially known as a swing

wing. It is of prime importance to optimize the morphing wing for conflicting multi-objectives of weight, aerodynamics, structure and actuation [2]. Morphing imposes a cost on the system with the advantages they bring in. Table 1 below briefly highlights the advantages and the challenges in terms of the cost of the system. This cost is generally associated with the morphing skin requirement to adapt the morphing mechanism and aerodynamic force distribution [3].

**Table 1.** Wing Morphing and its effect.

Morphing Type	Performance Effects	Benefit	Cost
Sweep	Drag-divergence, Mach number	Maneuvers, high-speed flight	Lower lift coefficient, higher weight
Cant	Lateral stability	Positive increases roll	Decrease maneuverability
Twist	Lift, Drag	Aerodynamic force control	Wing torsional rigidity
Span	Aspect Ratio, Wing loading	Shorter span maneuverability	Wing root moment

In most of the relevant literature, morphing wings have been shown to address a single rather than combined mechanisms (i.e., Spanwise, Cant, Sweep or Dihedral), except for the case of a compliant truss wing presented by Ramrakhyani et al. [4]. Finistauri [3], followed by Moosavian [5], have successfully implemented the parallel robot manipulator concept in morphing wing design, which can adapt to spanwise, dihedral and sweep mechanisms simultaneously per the flight condition requirements. Their base design is modular in nature and the number of modules has been determined based on the optimum mission requirement eliminating the redesign of wing for different missions. However, their work is limited to the design of such a morphing wing without any structural and/or aerodynamic analysis. The present work is aimed at performing the dynamic analysis of the morphing wing, developed by Moosavian in order to ultimately assess their aeroelastic behavior. Such analysis is deemed to highlight the main dynamic issues and the resolution of these wings with the purpose of predicting the fatigue life and reliability of the design.

It is required to investigate the truss analysis of the variable geometry truss mechanism applied to the re-configurable modular morphing wing design, based on a parallel robot that efficiently represents the dynamic behavior of the morphing wing design as conceived by Moosavian [5] and Finistauri [3]. It is imperative to study the structural response after the morphing mechanism has been implemented. However, current work will treat the structural members of the morphing mechanism as beams.

Objectives of the current report encompass the following. To:

- Compute the natural frequencies and mode shapes of the modular morphing wing, neglecting and including shear deformation and rotary inertia effects;
- Compare the in-plane (lead-lag) and out-of-plane (flapping) bending behaviors;
- Investigate the effect of morphed wing shape on the system's natural frequencies and modes;
- Study the effect of various topological configurations on the system's vibrational signature.

## 2. Theoretical Treatise

### 2.1. Modular Morphing Wing

The morphing wing analysed in this study is modular in nature. Each module consists of eight load bearing structural members and two wing ribs. Four of these load bearing members are active, controlled by actuators, and the other four are passive. Two optimal topological configurations, obtained through kinematic analysis presented by Finistauri and Moosavian [3,5], are investigated here. Active structural members are connected diagonally to the others, as presented in Figures 1 and 2. The two optimal topological configurations, termed Topology 1 and Topology 2, are illustrated in simplified forms in Figures 3 and 4, respectively. In each module, eight load bearing structural members are connected to each other and to the wing ribs through spherical (eye-bolt) joints. Four of these members are active, controlled by actuators, as shown by the mechanism in Figure 5.

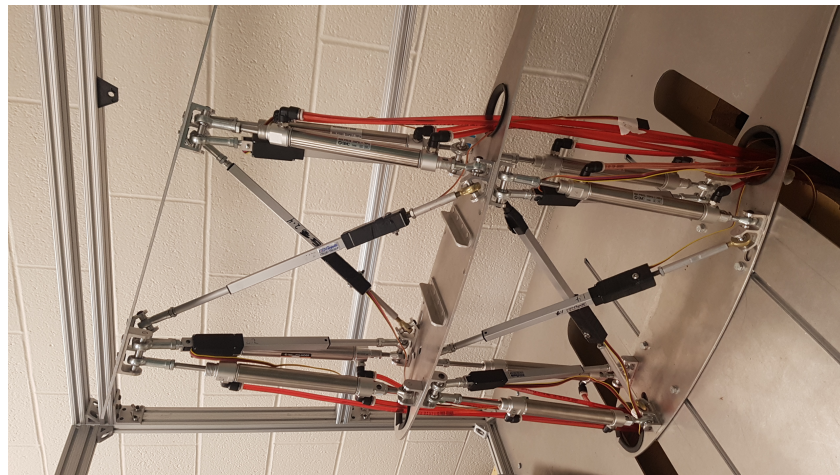


Figure 1. Reconfigurable modular morphing wing, view 1.

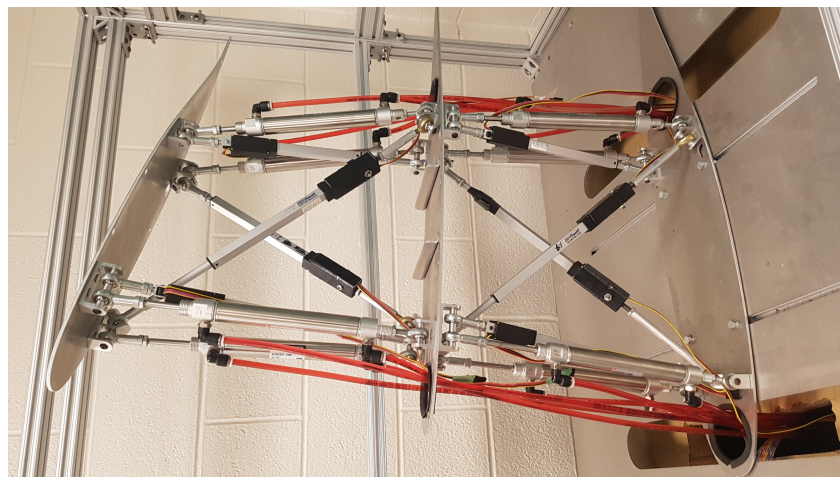


Figure 2. Reconfigurable modular morphing wing, view 2.

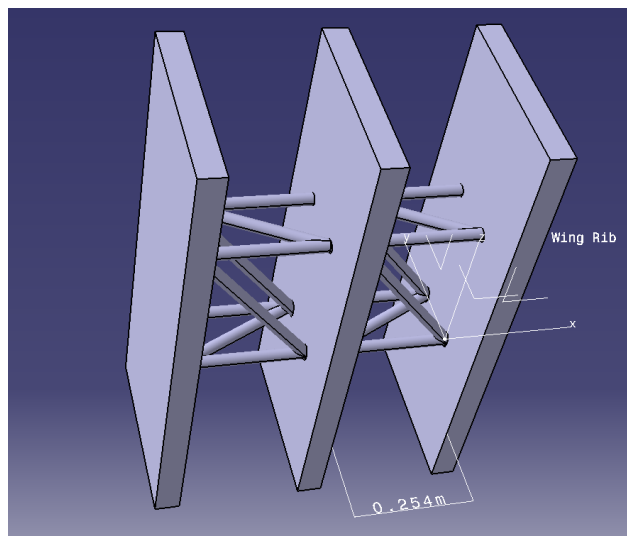
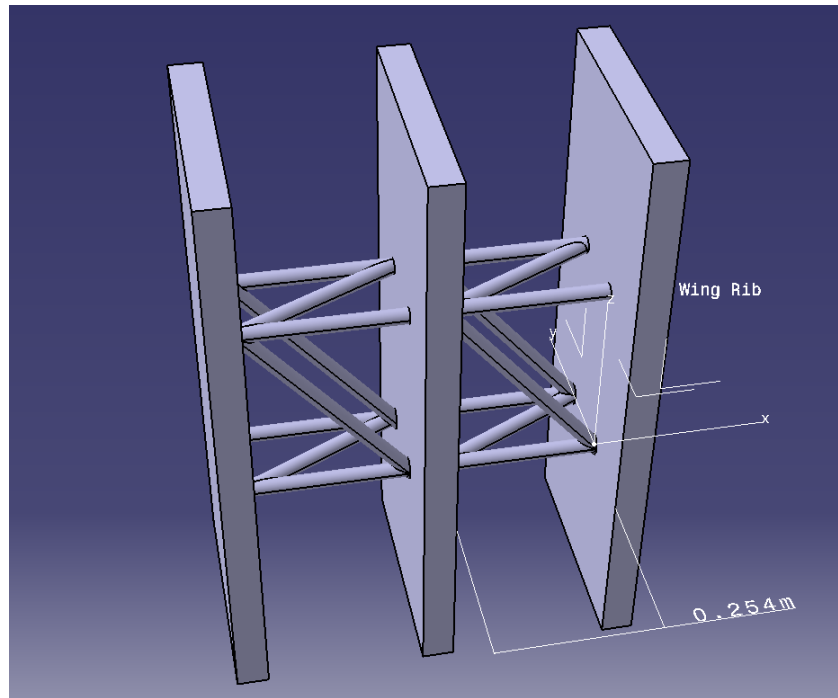
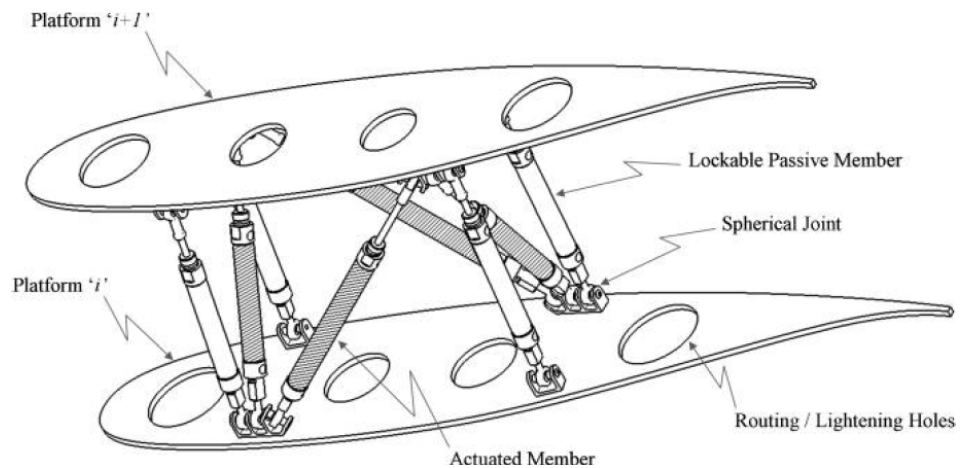


Figure 3. Configuration of structural element connections in morphing Wing, Topology 1.



**Figure 4.** Configuration of structural element connections in morphing wing, Topology 2.



**Figure 5.** Mechanism of the reconfigurable morphing wing, Topology 1 [6].

With these optimal topologies, various wing morphing configurations can be achieved including spanwise extension, dihedral, and sweep motion. A detailed procedure for obtaining the various morphing configuration is outlined by Moosavian [6].

2.2. Members’ Equations of Motion

Consider a beam in *xy* plane. By considering beams with considerable lateral dimensions comparable to axial dimension, the cross-section plane does not remain perpendicular to the neutral axis due to the shear deformation part  $\zeta(x)$  in addition to bending  $\phi(x)$ . This type of beam is generally referred to as a Timoshenko beam. Therefore, for a deflected Timoshenko beam at a section, the slope can be written as [7]:

$$\frac{dv}{dx} = \phi(x) + \zeta(x). \tag{1}$$

This makes the moment equation as follows:

$$M(x) = EI \frac{d\phi(x)}{dx}. \tag{2}$$

The relation between shear force and shear deformation can be written as:

$$V(x) = \kappa_s A G \zeta(x), \tag{3}$$

where  $\kappa_s A = A_s$  is the shear area.  $A_s$  for the solid circular cross-section is 0.9.

The resulting governing equations of the Timoshenko beam with a varying cross-section can be written as:

$$G \kappa_s \left[ \frac{\partial A}{\partial x} (\phi(x) - \frac{\partial v}{\partial x}) + A \left( \frac{\partial \phi}{\partial x} - \frac{\partial^2 v}{\partial x^2} \right) \right] + \rho A \frac{\partial^2 v}{\partial t^2} = q(x, t), \tag{4}$$

$$G A \kappa_s \left[ \frac{\partial v}{\partial x} - \phi \right] + E \left[ \frac{\partial I}{\partial x} \frac{\partial \phi}{\partial x} + I \frac{\partial^2 \phi}{\partial x^2} \right] = \rho I \frac{\partial^2 \phi}{\partial t^2}. \tag{5}$$

In the above equation,  $q$  is the distributed load on the beam. For a constant thickness Timoshenko beam, governing Equations (4) and (5) reduce to:

$$G A \kappa_s \left[ \frac{\partial^2 v}{\partial x^2} - \frac{\partial \phi}{\partial x} \right] = \rho A \frac{\partial^2 v}{\partial t^2} - q(x, t) \tag{6}$$

$$E I \left[ \frac{\partial^2 \phi}{\partial x^2} \right] + G A \kappa_s \left[ \frac{\partial v}{\partial x} - \phi \right] = \rho I \frac{\partial^2 \phi}{\partial t^2}. \tag{7}$$

Therefore, by using the standard Finite Element Methodology (FEM) [8], the stiffness matrix of the Timoshenko beam element of length  $L$  in 2D bending can be obtained from the static case, and is written as follows:

$$[k] = \frac{EI}{L^3(1 + \psi)} \begin{bmatrix} 12 & 6L & -12 & 6L \\ 6L & (4 + \psi)L^2 & -6L & (2 - \psi)L^2 \\ -12 & -6L & 12 & -6L \\ 6L & (2 - \psi)L^2 & -6L & (4 + \psi)L^2 \end{bmatrix} \tag{8}$$

where  $\psi = 12 \frac{EI}{\kappa_s A G L^2}$ .

The consistent mass matrix for the Timoshenko beams, including rotary inertia effect, can be obtained using the energy based formulation as presented by Davis et al. [9], as follows:

$$m = \rho A [X]^{-t} [H] [X], \tag{9}$$

where  $[H]$  is given below:

$$[H] = \begin{bmatrix} \frac{L^7}{252} + \gamma \left( \frac{L^5}{20} + \frac{L^3 \beta}{3} + \frac{L}{\beta^2} \right) & & & & \\ \frac{L^6}{72} + \gamma \left( \frac{L^4}{8} + \frac{L^2 \beta}{2} \right) & \frac{L^5}{20} + \frac{\gamma L^3}{3} & & & \text{Symmetrical} \\ \frac{L^5}{30} + \gamma \left( \frac{L^3}{6} + L \right) & \frac{L^4}{8} + \frac{\gamma L^2}{2} & \frac{L^3}{3} + \gamma L & & \\ \frac{L^4}{24} & \frac{L^3}{6} & \frac{L^2}{2} & & L, \end{bmatrix} \tag{10}$$

and  $[X]$  is given as:

$$[X] = \frac{EI}{L^3(1 + \psi)} \begin{bmatrix} 0 & 0 & 0 & 1 \\ \beta & 0 & 1 & 0 \\ \frac{L^3}{6} & \frac{L^2}{2} & L & 1 \\ \frac{L^2}{2} + \beta & L & 1 & 0, \end{bmatrix} \tag{11}$$

with  $\beta = \frac{EI}{\kappa_s A G}$  and  $\gamma = \frac{I}{A}$ .

By ignoring shear deformation and rotary inertia, Timoshenko beams are reduced to Euler–Bernoulli beams.

### 2.3. Beams with Hinged Nodes

A beam that has an internal hinge behaves as two beams connected at the hinge with a two-valued slope at the hinge in both transverse directions and a two-valued twisting angle. The bending slope of each beam at the hinge can be obtained from the deflections at the hinged node of the corresponding beam. Following the procedure outlined by Logan [8] by partitioning the original elemental matrix, if the hinged node is the second node (right node) of a beam element, the condensed stiffness matrix,  $[K_{c2}]$ , of that element can be obtained as follows:

$$[k_{c2}] = \begin{bmatrix} k_{11} - \frac{k_{14}^2}{k_{44}} & k_{12} - \frac{k_{14}k_{42}}{k_{44}} & k_{13} - \frac{k_{14}k_{43}}{k_{44}} \\ k_{21} - \frac{k_{24}k_{41}}{k_{44}} & k_{22} - \frac{k_{24}^2}{k_{44}} & k_{23} - \frac{k_{24}k_{43}}{k_{44}} \\ k_{31} - \frac{k_{34}k_{41}}{k_{44}} & k_{32} - \frac{k_{34}k_{42}}{k_{44}} & k_{33} - \frac{k_{34}^2}{k_{44}} \end{bmatrix} \quad (12)$$

where  $k_{ij}$  are original components of the stiffness matrix of the Timoshenko beam element in 2D bending. For the first node (left node) of the beam element to be hinged, then the condensed stiffness matrix  $[K_{c1}]$  of that element can be obtained as follows:

$$[k_{c1}] = \begin{bmatrix} k_{11} - \frac{k_{12}^2}{k_{22}} & k_{13} - \frac{k_{12}k_{23}}{k_{22}} & k_{14} - \frac{k_{12}k_{24}}{k_{22}} \\ k_{31} - \frac{k_{32}k_{21}}{k_{22}} & k_{33} - \frac{k_{23}^2}{k_{22}} & k_{34} - \frac{k_{32}k_{24}}{k_{22}} \\ k_{41} - \frac{k_{42}k_{21}}{k_{22}} & k_{43} - \frac{k_{42}k_{23}}{k_{22}} & k_{44} - \frac{k_{24}^2}{k_{22}} \end{bmatrix} \quad (13)$$

The condensed mass matrices can be obtained in a similar way.

### 2.4. Conventional Modal Analysis

Modal analysis is performed using the conventional FEM based on the equations of motion written as:

$$[M]\ddot{d} + [K]d = 0, \quad (14)$$

where  $d$  is the displacement vector, with  $d_i$  for the nodal DOFs written as:

$$d_i = \begin{bmatrix} v_i \\ \phi_i \end{bmatrix} \quad (15)$$

and  $[M]$  and  $[K]$  are the assembled mass and stiffness matrices of the system, respectively. Here, the 2 DOF per node is assumed for simplicity. The following harmonic solutions ((16) and (17)) are used for the governing Equations (6) and (7),

$$v = v_0 e^{-i\omega t} \quad (16)$$

$$\phi = \phi_0 e^{-i\omega t}. \quad (17)$$

By using these harmonic solutions and letting  $q = 0$ , along with stiffness and mass matrices of the Timoshenko beam, the system's linear eigenvalue problem (18) is obtained as given below.

$$[K - \omega^2 M]d = 0. \quad (18)$$

Therefore, circular natural frequency  $\omega$  (eigenvalue) and corresponding mode shape (eigenvector)  $d$  can be obtained by solving the linear eigensystem by solving Equation (18).

### 2.5. Modal Analysis by Dynamic Stiffness Matrix Method

By applying the continuous mass and stiffness distribution along the beam, the analytical solution, the Dynamic Stiffness Matrix (DSM) methodology outlined by Wittrick and Williams [10,11], results in the following nonlinear eigensystem.

$$[K(\omega)]d = 0. \quad (19)$$

Graphically (plotting  $|K(\omega)|$  for various values of  $\omega$ ), by finding the zero-crossings obtained either by the determinant  $|K(\omega)| = 0$  or  $|K(\omega)| = \infty$ , natural modes of the system can be extracted. DSM for the bending of the Timoshenko beam is given by Banerjee [12]. Axial and torsional components of DSM are given by Peng [13] and Anusmita [14], respectively. Mode finding techniques (i.e., bisection technique) proposed by Wittrick and Williams [10] can also be employed to obtain the free vibration frequencies and modes of the beam. The number of modes passed by a set frequency  $\omega = \omega^*$  can be computed by:

$$j = j_0 + \text{sgn}\{K\}, \quad (20)$$

where  $j_0$  are the natural frequencies lying between 0 and  $\omega^*$  when all the elements are subjected to fixed-fixed boundary conditions, and  $\text{sgn}\{K\}$  is the number of negative signs on the main diagonal of upper triangular matrix  $K^\Delta$  of the DSM,  $K(\omega)$  is obtained by Gaussian elimination method without row or column interchange. The detailed procedure of finding the required natural frequencies using DSM is explained in detail by Williams and Wittrick ([10,11]).

### 3. Methodology

In this work, two modules of the morphing wing are considered for the modal analysis. Each load bearing structural member in a module is modeled as a beam. Each beam is divided into a number of Timoshenko or Euler-Bernoulli beam elements (Equations (8) with six degrees of freedom per node, and (9)). The spherical (eye-bolt) joints between wing rib and load bearing structural members (beams) are modeled as hinged joints in 3D to transmit only the linear motions along three coordinate axes, by suppressing the transfer of rotational motions between the connected structural members (Equations (12) and (13)). Based on the Timoshenko beam theory and the hinged joint in 3D (representing the spherical joint) analysis and DSM with spherical joints, presented in the previous section, modal analysis of the modular morphing wing with two modules will be performed. However, modules can be added per mission requirements. The following are the assumptions applied here:

- Wing ribs can be represented by five structural beam elements connecting eight other beam/bars in each module;
- Stiffness of structural members representing wing ribs is of the order of 1000 of that of structural members of the module;
- All structural beams are initially straight and un-stressed;
- Plane section remains plane during bending, but is no longer perpendicular to the neutral axis;
- All structural elements are perfectly elastic, homogeneous and isotropic;
- Upon the spanwise expansion, the diameter of each structural member can be assumed uniform and computed based on the constant mass of the member.

Conventional Finite Element Analysis (FEA) using Timoshenko and Euler-Bernoulli beam theories is applied to form the assembled stiffness and mass matrices of the morphing wing. For the end elements of each beam, condensed stiffness and mass matrices are applied using the hinged nodal analysis presented previously. Fixed boundary conditions are applied for the right end of the first module, representing attachment to the fuselage. The eigenvalue problem, presented in Equation (18), is solved to perform the modal analysis of the assembled mass and stiffness matrices of the whole system. Therefore, the first few frequencies and the corresponding mode shapes are obtained. To validate

the conventional FEA approach, Dynamic Stiffness Matrix (DSM) is applied to compute the matrix  $K(\omega)$  for the whole system by assembling individual matrices. To obtain any natural frequency number and its value, a high frequency is given as a set frequency. Then, by the application of the bi-section method, any required natural frequency is computed, within a given tolerance, below the set frequency by using Equations (19) and (20). This obtained frequency is also checked by plotting the  $|K(\omega)|$  against  $\omega$  and finding the zero-crossings. After validation of the computed natural frequencies, various parametric analysis are performed for observing the effect of material, spanwise expansion and the effect of topology of the modular design (configuration of connecting beams with each other in module) using the conventional FEA approach. For spanwise expansion cases, the total mass of the beams will remain unchanged due to the telescopic characteristic of the beams used here. However, the stiffness of each beam will vary and is computed. The effect of beams extension will be incorporated by changing the effective diameters of beams while keeping the mass constant.

#### 4. Numerical Simulations and Discussions

Modal analysis of a reconfigurable modular design of a morphing wing is presented. Before presenting the results of the modular wing, a simple simulation of two beams connected through a hinged node is simulated here. Based on this simple case, more complex cases of a frame of beams will be presented.

##### 4.1. Modal Analysis of Two Beams Connected by a Hinged Joint

Two horizontal Euler–Bernoulli beams, made of steel (Table 2) and 0.254 m long with a diameter of 0.0254 m, are connected by an hinged node at the middle. Fixed–Fixed beam analysis with a hinged node at their joint is executed here. Each beam is discretized into 30 finite elements, and each node has 6-DOF. Therefore, a spherical joint at their interface is simulated by employing hinged node in 3D. FEM–based modal analysis is performed, and the first computed 10 modes are tabulated in Table 3. The results are also validated against those obtained from commercial software, Ansys.

**Table 2.** Mechanical Properties of Steel.

Material	Density kg/m <sup>3</sup>	Modulus of Elasticity Pa	Poisson Ratio	Shear Modulus Pa
Low Carbon Steel	7750.4	$1.8616 \times 10^{11}$	0.3	$7.16 \times 10^{10}$

**Table 3.** Natural Frequencies,  $\omega$ (rad/s), of Two Euler–Bernoulli Beams Analysis with Hinged node.

Mode	1	2	3	4	5	6	7	8	9	10
FEM	1781.8	1781.8	7441	7452.5	11159	11182	19234	19234	24118	24257
Ansys	1684.94	1684.94	7223.50	7223.50	10,213.30	10,213.30	18,794.43	18,794.43	22,369.11	22,369.11
Difference (%)	5.75	5.75	3.01	3.17	9.26	9.48	2.34	2.34	7.82	8.44

The first four mode shapes of the above-mentioned case are also shown in Figures 6–9, where ordinate and abscissa axes are in meters. It is clear from these figures and Table 3 that beams present repeated modes in horizontal and vertical planes. Therefore, it can be observed that the existence of the hinged node represents the fixed–fixed case as two cantilever beams. However, their natural frequencies become different compared to the corresponding independent cantilever case. This is due to the translatory motion transfer across the spherical joint.

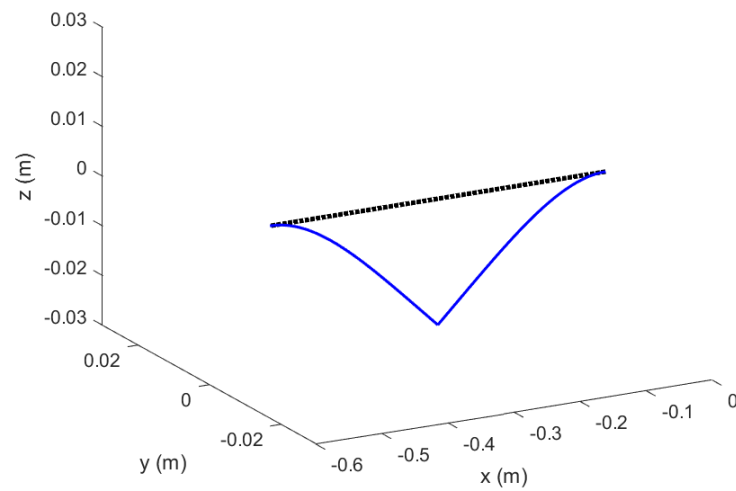


**Figure 6.** Mode 1 (out-of-plane/flapping) of two Euler-Bernoulli Beams connected through hinged joint.

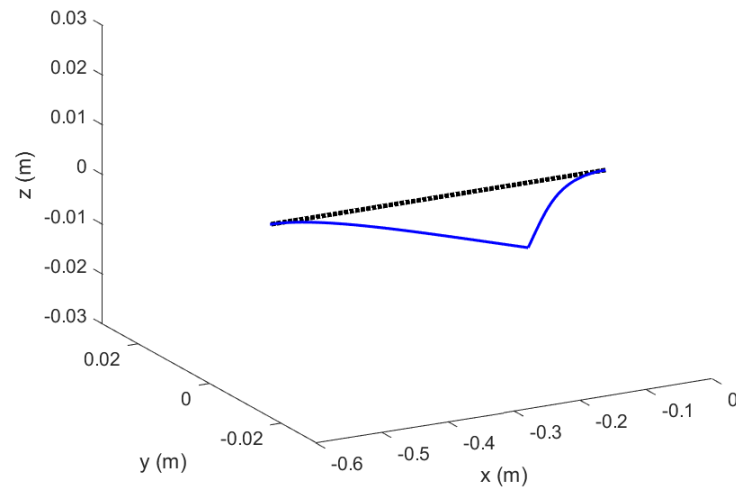


**Figure 7.** Mode 2 (in-plane/lead-lag) of two Euler-Bernoulli Beams connected through hinged joint.

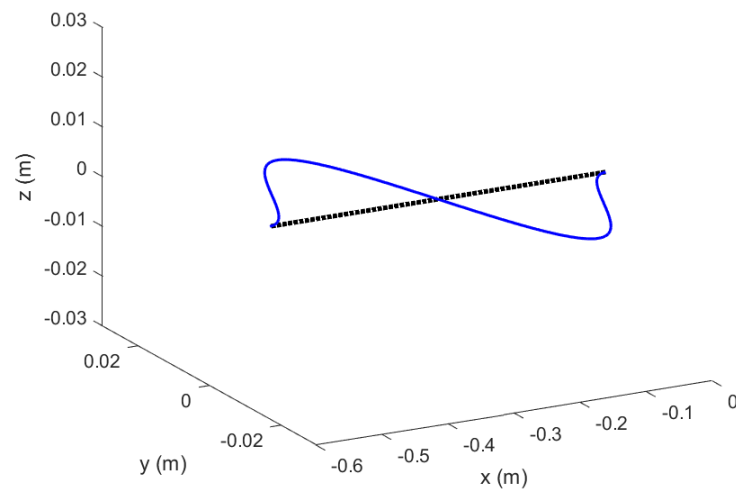


**Figure 8.** Mode 3 (out-of-plane/flapping) of two Euler-Bernoulli Beams connected through hinged joint.

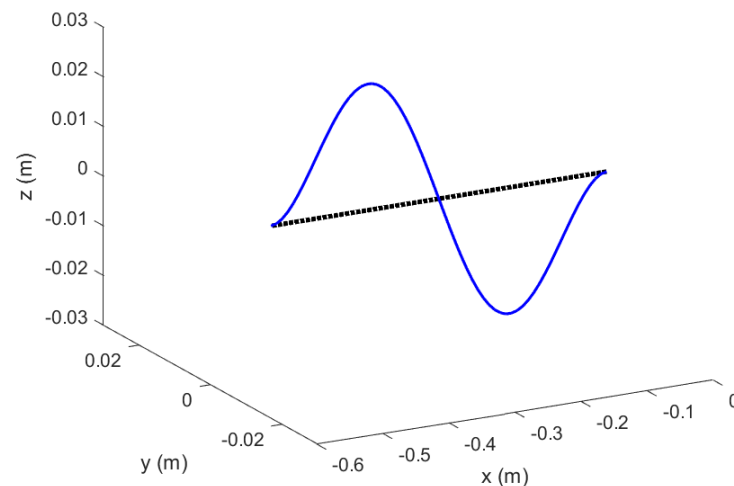


**Figure 9.** Mode 4 (in-plane/lead-lag) of two Euler–Bernoulli Beams connected through hinged joint.

#### 4.2. Modal Analysis of the Two-Module Morphing Wing, Topology 1

Based on the initial simple case of two beams connected by a spherical joint at their interface, now simulations are executed for the morphing wing's modal analysis in the original configuration (i.e., without expansion of morphed shape). As also discussed earlier in this paper, each wing design is composed of two modules, each composed of eight structural beams and two ribs. Each rib is also represented by five beams, i.e., there are 26 beams in total. Diameter of each beam in un-morphed configuration is 0.0254 m. The distance between two wing ribs is 0.254 m and the distance between two horizontal beams (in x-y plane) along the z-axis is 0.3048 m (refer to Figure 3). Each mode shape is presented individually for clarity, as combining five mode shapes of these 26 beams would make the presentation very complicated, as each mode shape becomes indiscernible from other mode shapes. Moreover, the 3-dimensional motion (lift, bending, and twisting) will be completely masked by mode shape overlapping.

##### 4.2.1. Application of Euler–Bernoulli Beam Theory

Euler–Bernoulli beam analysis is performed here. Mechanical properties for these beams are the same as those used in the previous subsection. First, to obtain a benchmark simulation of the response of beams, no hinged node is considered. Therefore, no slope discontinuity is expected at the nodes. Each load carrying beam is discretized into 30 elements (for converged solution, shown later) and each node has 6-DOF. The results of conventional FEM-based modal analysis are presented here. The first ten modes obtained from conventional FEM and validated by DSM are tabulated in Table 4. Differences less than 0.02% are observed. The un-morphed wing with two modules, without deformation, is presented in Figure 10. The two vertical rectangular members with five beams (four on circumference and one diagonal) represent simplified wing ribs. The first five mode shapes of the wing (presented in Figure 10) are presented in Figures 11–15. All the  $x, y, z$  coordinates are in meters. Evident from these figures, vertical and horizontal motion of wing rib is observed in the first mode. However, horizontal motion is predominant. Twisting and bending coupling is also observed in the second mode. Vertical motion along with bending in internally diagonal beams is observed in the third mode. Interestingly, the fourth and fifth modes clearly present flexural motion in internal diagonal beams. Graphical representation of the change of sign (zero-crossing) of the determinant,  $|k(\omega)|$  using DSM is depicted in Figure 16. Only the 10th and the 9th natural frequencies are represented here for the sake of brevity. The 9th natural frequency is shown in Figure 16b extracted by the detailed section given in Figure 16a. In finding the zero-crossing, the magnitude of  $|k(\omega)|$  is of no importance. Since, in DSM, the determinant  $|k(\omega)|$  changes

sign either at  $|k(\omega)| = 0$  or at  $|k(\omega)| = \infty$ , a multiplying factor of  $10^{-7}$  is used to limit the magnitude of  $|k(\omega)|$ .

**Table 4.** Natural Frequencies,  $\omega(rad/s)$  of Euler–Bernoulli Beam Analysis with no spherical joint in Topology 1, Original Configuration.

Mode	1	2	3	4	5	6	7	8	9	10
FEM	1909.5	3471.1	3590.5	4307.4	4372.5	4395.3	4419	4429.5	4507.7	4850.5
DSM	1910.4	3474.1	3586.4	4309.1	4372.6	4387.2	4411.6	4421.4	4509.3	4841.3
Difference (%)	0.05	0.09	0.119	0.04	0.0023	0.18	0.17	0.18	0.035	0.19

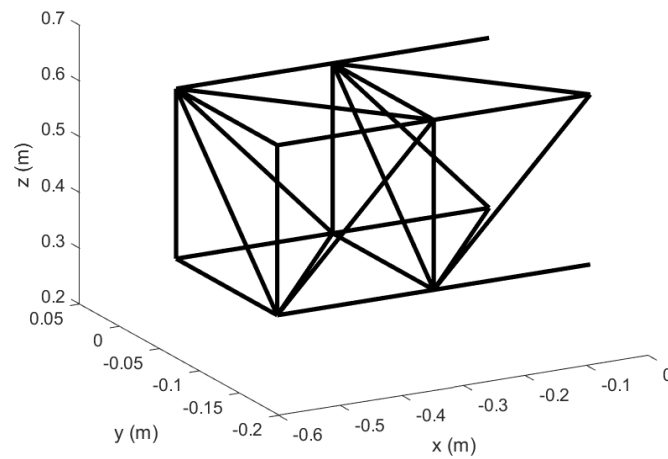


**Figure 10.** Un-morphed wing in Topology 1 with no hinged ends; original configuration.

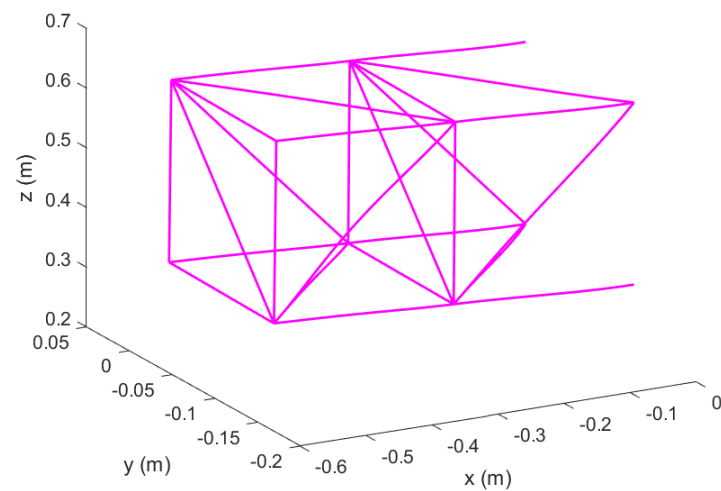


**Figure 11.** Mode 1 of Euler–Bernoulli Beams in Topology 1 with no hinged ends; original configuration.

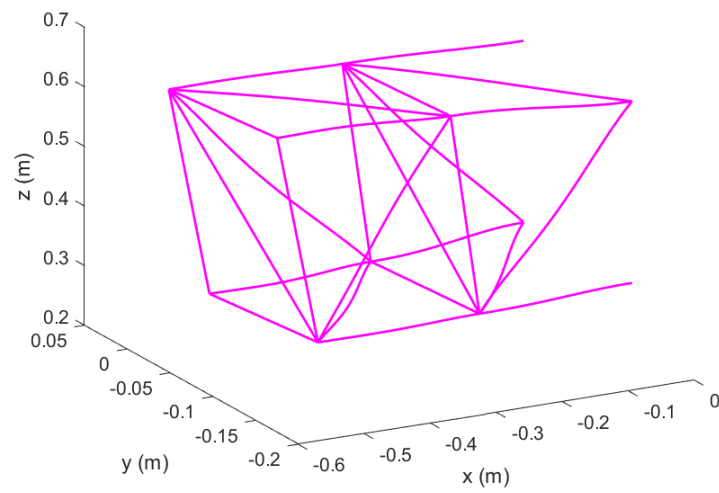


**Figure 12.** Mode 2 of Euler–Bernoulli Beams in Topology 1 with no hinged ends; original configuration.

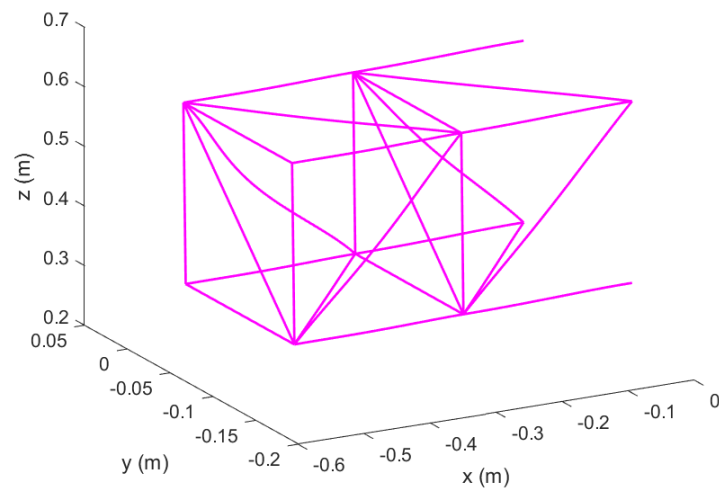


**Figure 13.** Mode 3 of Euler–Bernoulli Beams in Topology 1 with no hinged ends; original configuration.

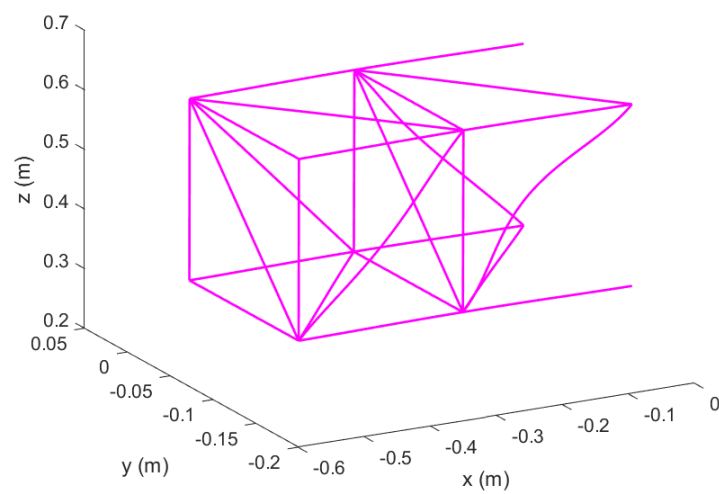


**Figure 14.** Mode 4 of Euler–Bernoulli Beams in Topology 1 with no hinged ends; original configuration.

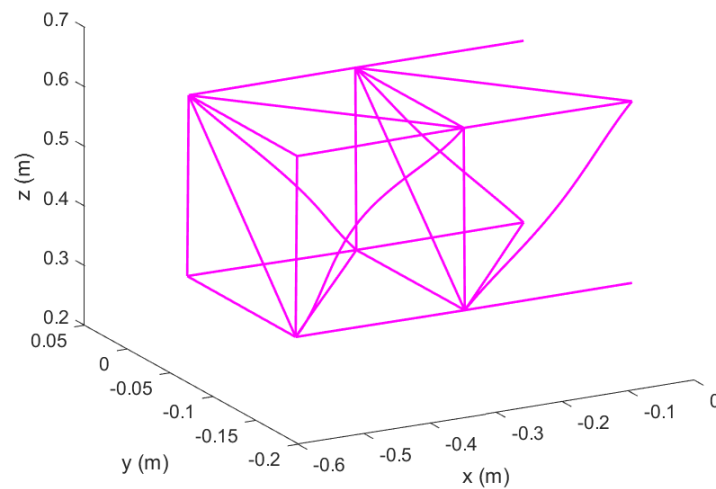


**Figure 15.** Mode 5 of Euler–Bernoulli Beams in Topology 1 with no hinged ends; original configuration.

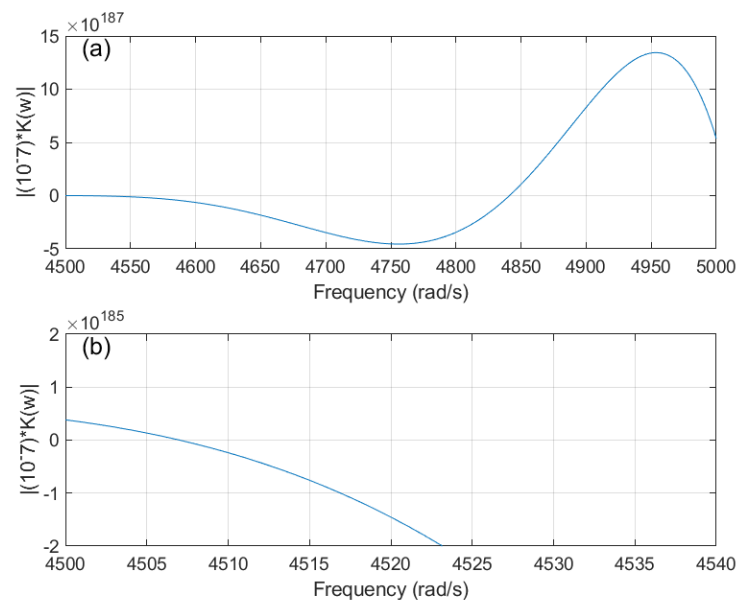


**Figure 16.** Dynamic Stiffness Matrix plot of Euler–Bernoulli Beams in Topology 1 with unhinged ends using DSM; original configuration (a) a selected region of natural frequencies showing zero-crossing at the 10th natural frequency (b) a detailed section showing zero-crossing at the 9th natural frequency.

After obtaining the frequency results with fixed-to-rib boundary conditions (i.e., with no hinge-noded end) and validating them against DSM, Euler–Bernoulli beams with both ends hinged (spherical joint) to the wing ribs are simulated in the un-morphed (base) configuration. Thirty elements per beam are considered for obtaining the converged solution, which will be shown later in this paper. The first ten natural frequencies are given in Table 5. Natural frequencies are reduced as compared to those without hinged nodes. It is noteworthy that differences with respect to DSM increased overall but still remains less than 2%. Convergence will be shown later in this section. The un-morphed wing with two modules and hinged (spherical) joints, without deformation, is presented in Figure 17. Comparing the modes shapes (presented in Figures 18–22) with those with no hinged ends, it is found that first mode shape qualitatively is the same in both cases, regardless of the magnitude, namely the coupled bending in both horizontal and vertical plane. However, internal diagonal beams undergo flexural motion in this case. Additionally, the second and third modes show some bending coupling along with more pronounced flexural motion in internal beams of the modules. No twist-bending coupling is observed in the first five

modes. Graphical representation of the change of sign (zero-crossing) of the determinant,  $|k(\omega)|$  using DSM is depicted in Figure 23. Only the 10th and the 9th natural frequencies are represented here for the sake of brevity. The 9th natural frequency is shown in Figure 23b obtained by the detailed section given in Figure 23a. Again, it is clear from the flexural motion of beams represented here that the structural load bearing members cannot be treated as truss elements.

**Table 5.** Natural Frequencies,  $\omega(rad/s)$  of Euler–Bernoulli Beam Analysis with Hinged ends in Topology 1, Original Configuration.

Mode	1	2	3	4	5	6	7	8	9	10
FEM	1549.6	1917.6	1923.6	1937.1	1945.7	1950.5	1953.3	1954.1	2498.5	2922.1
DSM	1533.7	1914.6	1923.3	1938	1946.8	1949.7	1949.7	1952.6	2465.3	2881.3
Difference (%)	1.04	0.16	0.02	0.05	0.06	0.04	0.18	0.08	1.35	1.42

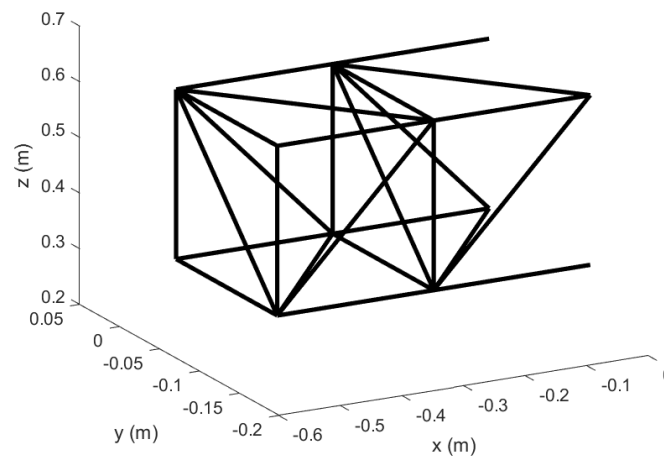


**Figure 17.** Un-morphed wing in Topology 1 with hinged ends; original configuration.

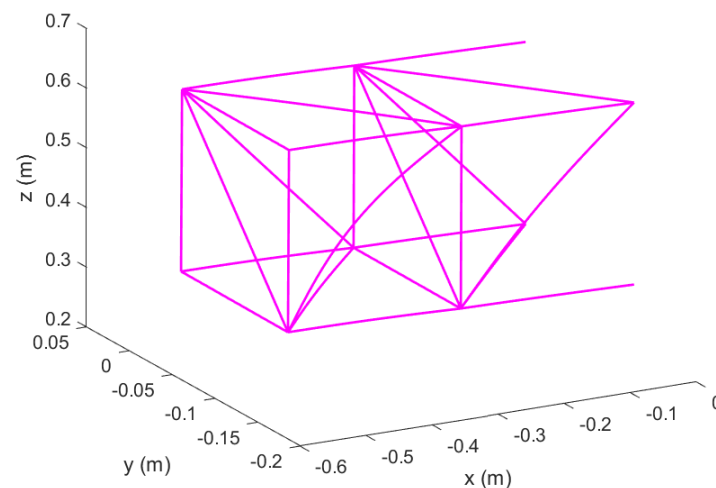


**Figure 18.** Mode 1 of Euler–Bernoulli Beams in Topology 1 with hinged ends; original configuration.

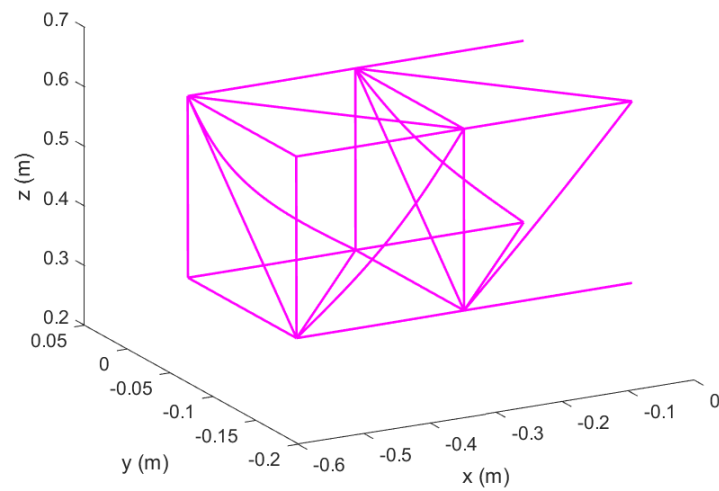


**Figure 19.** Mode 2 of Euler-Bernoulli Beams in Topology 1 with hinged ends; original configuration.

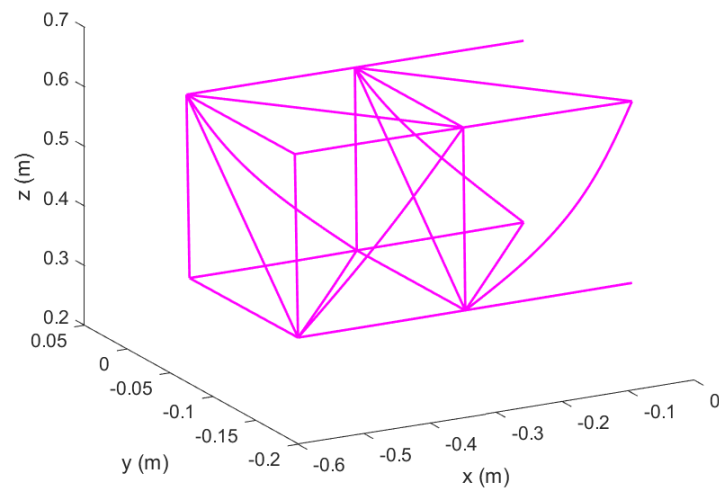


**Figure 20.** Mode 3 of Euler-Bernoulli Beams in Topology 1 with hinged ends; original configuration.

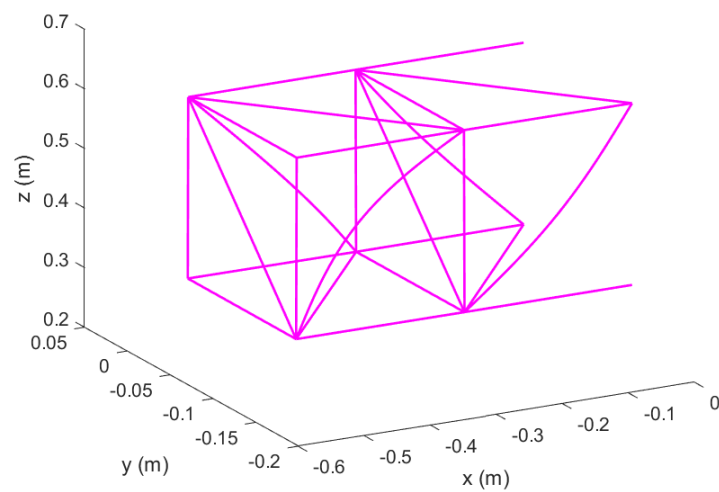


**Figure 21.** Mode 4 of Euler-Bernoulli Beams in Topology 1 with hinged ends; original configuration.

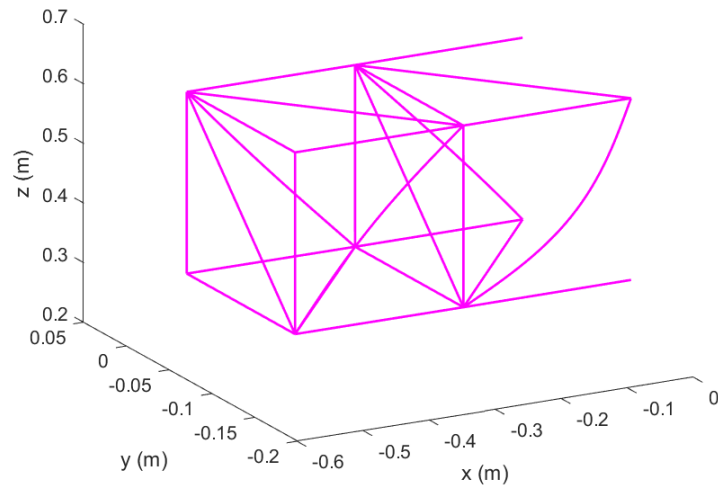


Figure 22. Mode 5 of Euler–Bernoulli Beams in Topology 1 with hinged ends; original configuration.

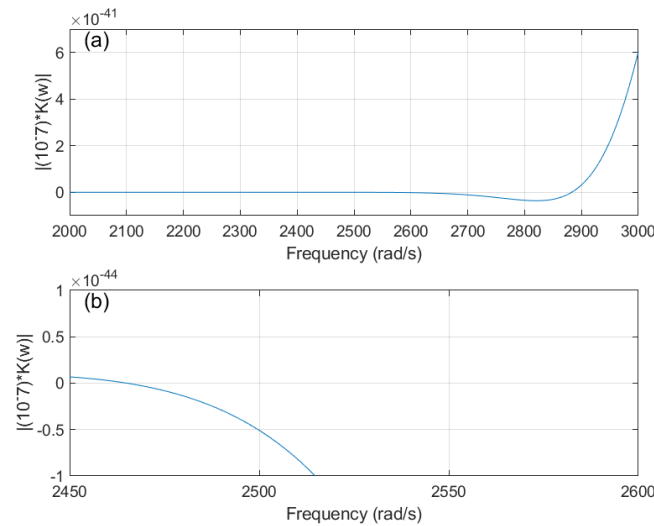


Figure 23. Dynamic Stiffness Matrix plot of Euler–Bernoulli Beams in Topology 1 with hinged ends using DSM; original configuration (a) a selected region of natural frequencies showing zero-crossing at the 10th natural frequency (b) a detailed section showing zero-crossing at the 9th natural frequency.

#### 4.2.2. Application of Timoshenko beam Theory

After Euler–Bernoulli beam analysis, Timoshenko beams are applied as the structural members for each module in the morphing wing by considering hinged ends (spherical joints) at both ends of all beams. Each beam is discretized into 30 elements (converged solution) and 6 DOF is applied at each node as before. Modal analysis is performed for this case and validated with the corresponding DSM case. Results are tabulated for the first ten modes in Table 6.

Table 6. Natural Frequencies,  $\omega$ (rad/s) of Timoshenko beam Analysis with Hinged ends in Topology 1, original configuration.

Mode	1	2	3	4	5	6	7	8	9	10
FEM	1528.9	1915.7	1927.2	1932.4	1937.7	1967.6	1974.5	1975.4	2462.6	2862.4
DSM	1530.8	1905.8	1911.6	1926.3	1935.1	1938	1940.9	1940.9	2453.6	2872.6
Difference (%)	0.12	0.52	0.82	0.32	0.13	1.53	1.73	1.78	0.37	0.36

Plot of the DSM simulations showing the representative 10th and 9th natural frequencies, depicted by zero-crossings of the curve, is presented here in Figure 24.

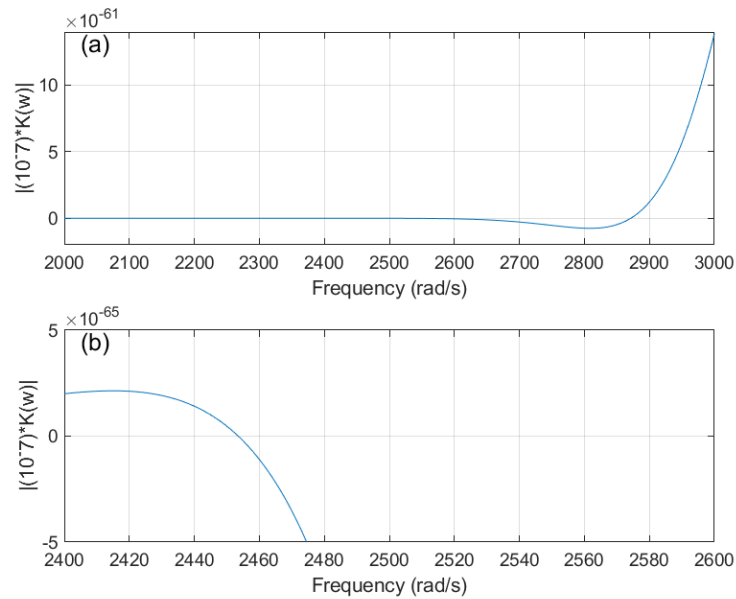


**Figure 24.** Mode Plot of Timoshenko beams in Topology 1 with hinged ends using DSM; original configuration (a) a selected region of natural frequencies showing zero-crossing at the 10th natural frequency (b) a detailed section showing zero-crossing at the 9th natural frequency.

The un-morphed wing with two modules and hinged (spherical) joints, without deformation, is presented in Figure 25. The first five mode shapes are presented here in Figures 26–30. Comparing with the corresponding Euler–Bernoulli beam case, it is observed that mode shapes are similar. However, it is found that natural frequencies are reduced in Timoshenko beam analysis. Moreover, this reduction increases with the increasing mode number. Natural frequencies are very close to each other though repeated modes are not observed. The differences with respect to DSM modes are very small in the converged solution, and is of the order of 1.8%. This reduction in natural frequencies is attributed to the inclusion of shear deformation and rotary inertia in the analysis.

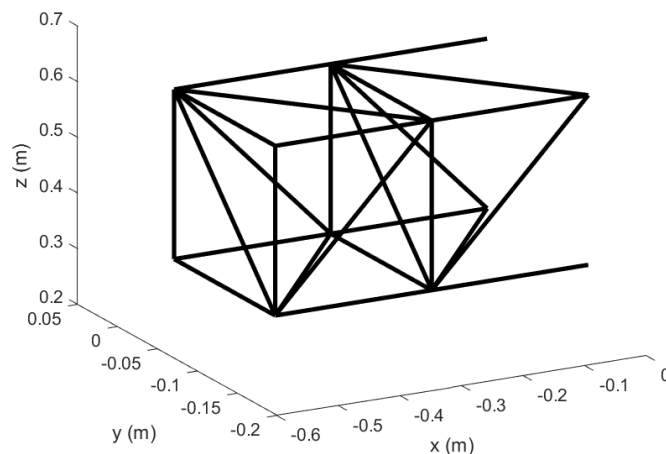


**Figure 25.** Un-morphed wing in Topology 1 with hinged ends; original configuration.

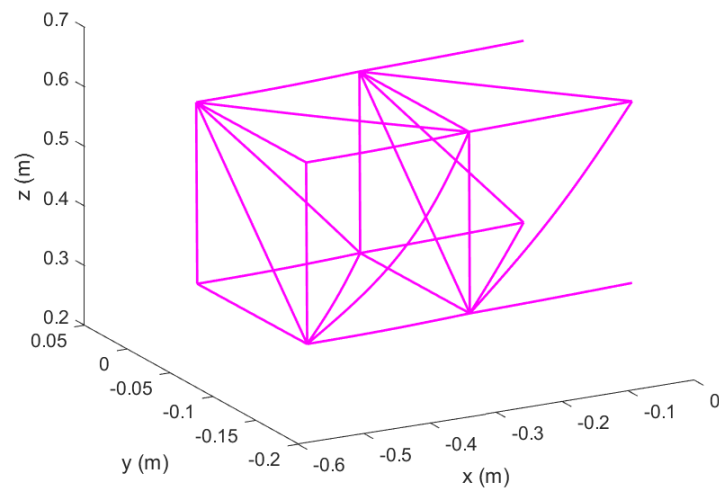


**Figure 26.** Mode 1 of Timoshenko beams in Topology 1 with hinged ends; original configuration.

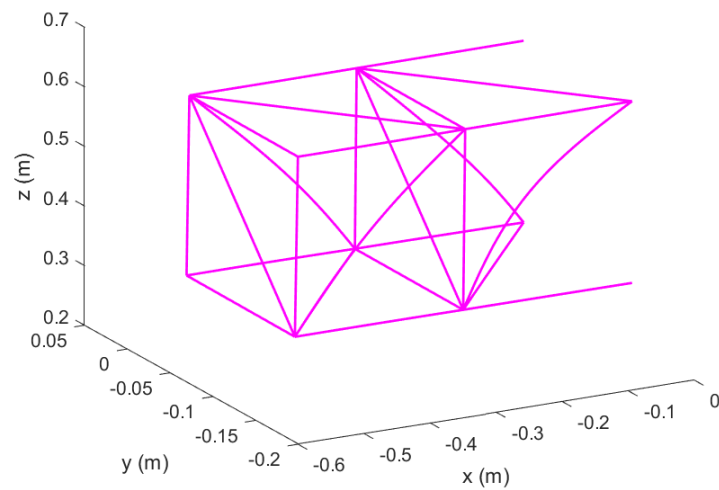


**Figure 27.** Mode 2 of Timoshenko beams in Topology 1 with hinged ends; original configuration.

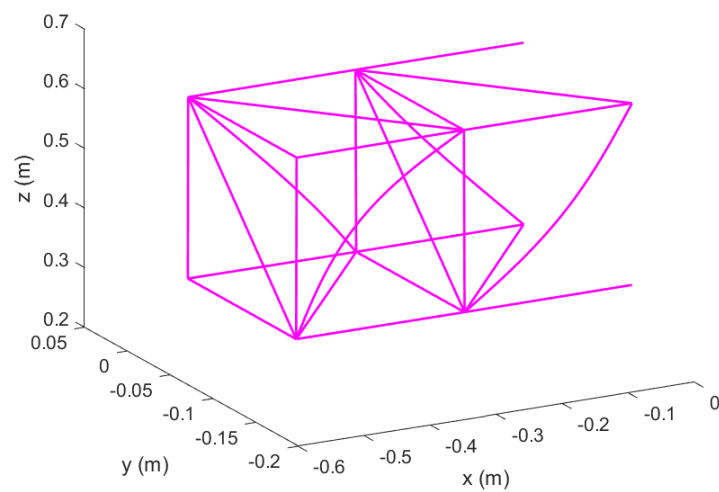


**Figure 28.** Mode 3 of Timoshenko beams in Topology 1 with hinged ends; original configuration.

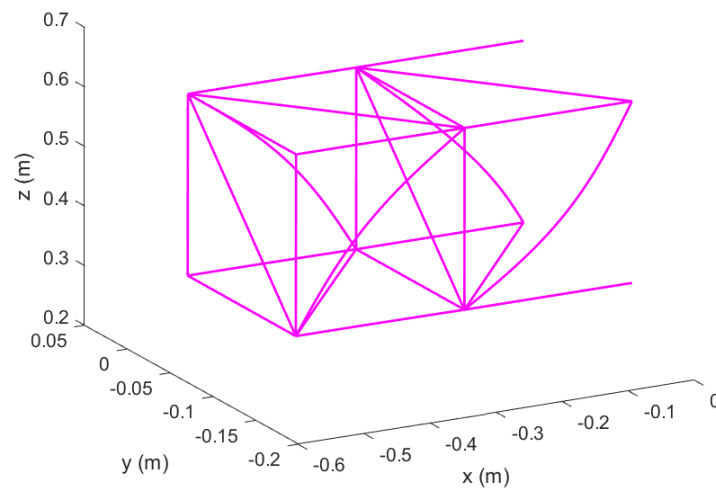


**Figure 29.** Mode 4 of Timoshenko beams in Topology 1 with hinged ends; original configuration.

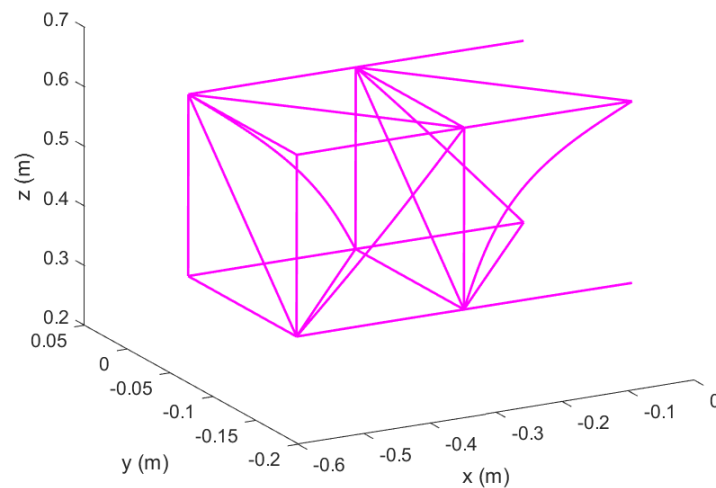


**Figure 30.** Mode 5 of Timoshenko beams in Topology 1 with hinged ends; original configuration.

#### 4.3. Convergence

A convergence study has been carried out for the Timoshenko beam-based modular wing model of topology 1 undergoing spanwise morphing of 12%. Results of the simulations for the first ten modes are plotted below in Figure 31. It is found that 30 elements per beam are sufficient for the converged solution.

#### 4.4. Effect of Spanwise Expansion

An analysis of the effect of spanwise expansion on the natural frequencies has been conducted here. The material used was steel as before, and the number of elements in each beam was 30. Each of two modules expands half of the required expansion. For every expansion case of the morphing wing, the diameter (therefore, area and moment of inertia) of each structural beam was calculated by keeping its corresponding mass constant. First, the effect on the first ten modes has been investigated and tabulated in Table 7. The morphed wing with two modules and hinged (spherical) joints for the representative expansion of 12% is depicted in Figure 32. Corresponding mode shapes for the first five modes undergoing the expansion of 12% are presented in Figures 33–37. It is found that spanwise expansion stiffness of the system decreases as evident by the lower natural frequencies compared to the un-morphed (original) configuration.

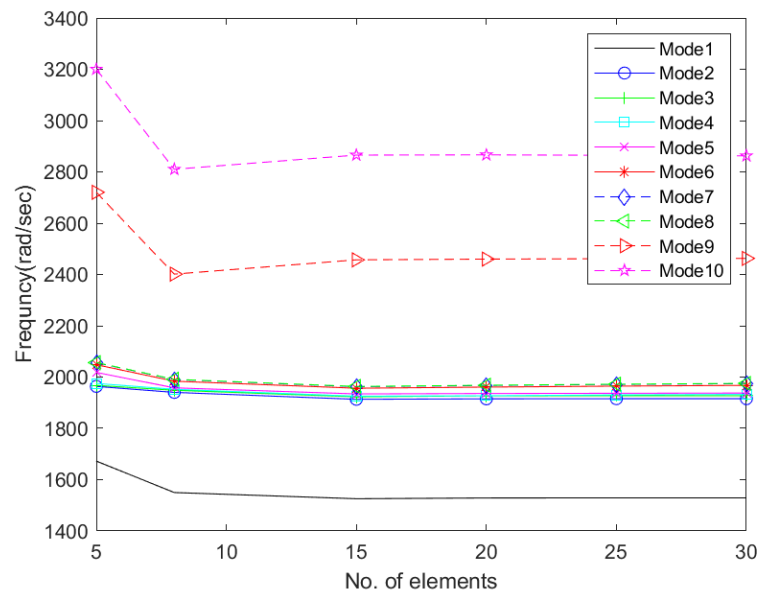


**Figure 31.** Convergence of natural frequencies of Timoshenko beams in Topology 1 with hinged ends.

**Table 7.** Natural Frequencies,  $\omega$  (rad/s) of Timoshenko beam Analysis with Hinged ends in Topology 1, 12% spanwise expanded configuration

Mode	1	2	3	4	5	6	7	8	9	10
FEM	1276.6	1690.3	1702.2	1703	1710.5	1735.7	1741.8	1742.6	2080.4	2376.8

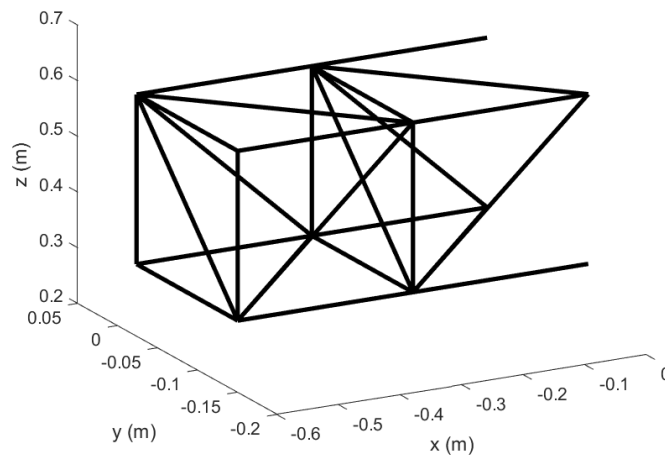


**Figure 32.** 12% Spanwise Expanded wing in Topology 1 with hinged ends; morphed configuration.

Moreover, the first ten natural frequencies for various expansion cases, ranging from 0 to 20% are extracted and presented in Table 8 and Figure 38. As can be observed, this variation is almost linear for the expansion cases studied here. It is also evident that natural frequencies corresponding to mode 2 to mode 8 are very close.

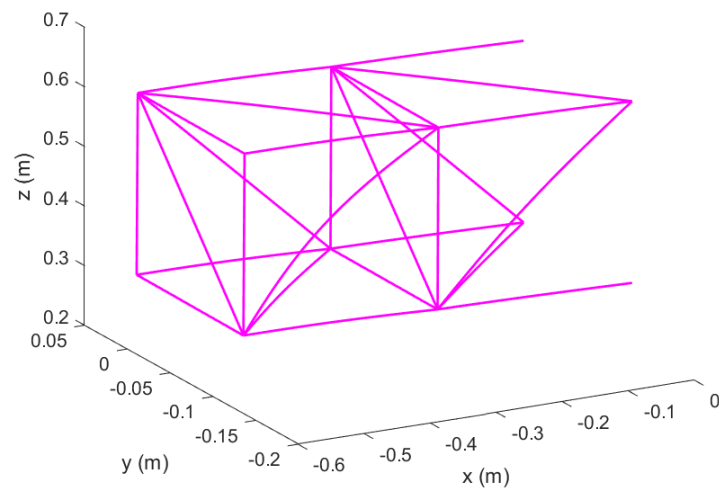


**Figure 33.** Mode 1 of Timoshenko beams in Topology 1 with hinged ends; spanwise expanded configuration.

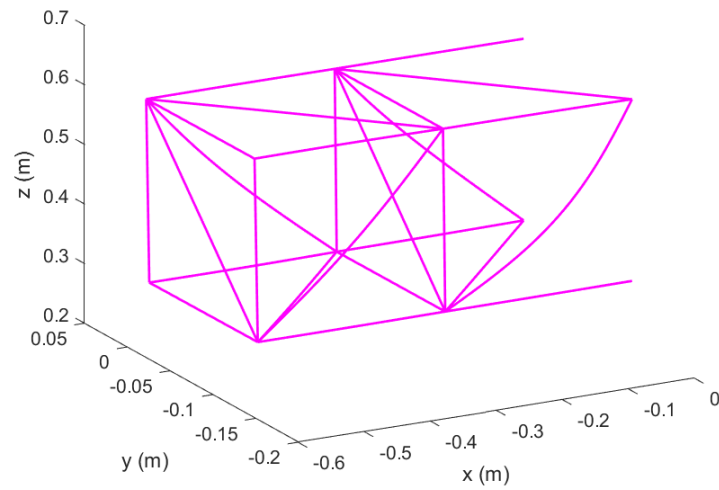


**Figure 34.** Mode 2 of Timoshenko beams in Topology 1 with hinged ends; spanwise expanded configuration.

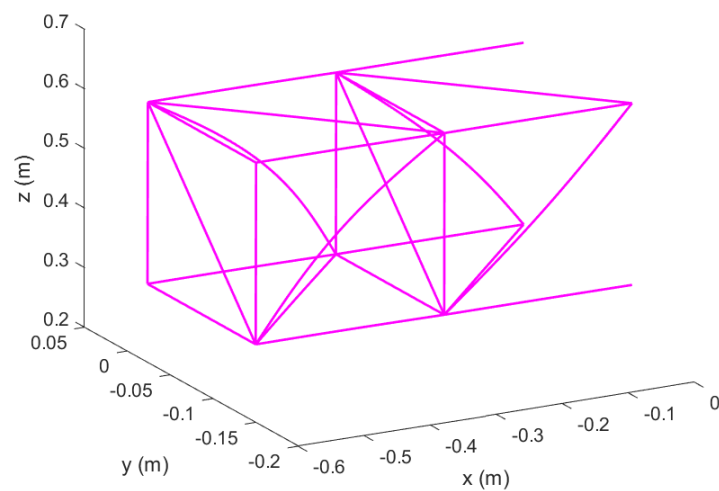


**Figure 35.** Mode 3 of Timoshenko beams in Topology 1 with hinged ends; spanwise expanded configuration.

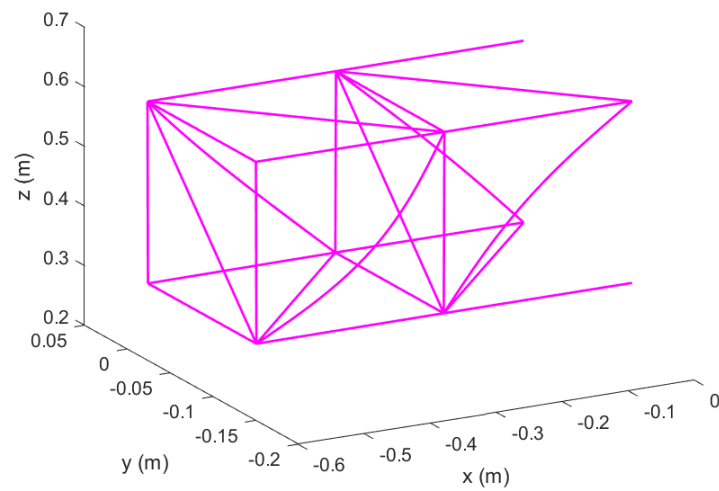


**Figure 36.** Mode 4 of Timoshenko beams in Topology 1 with hinged ends; spanwise expanded configuration.

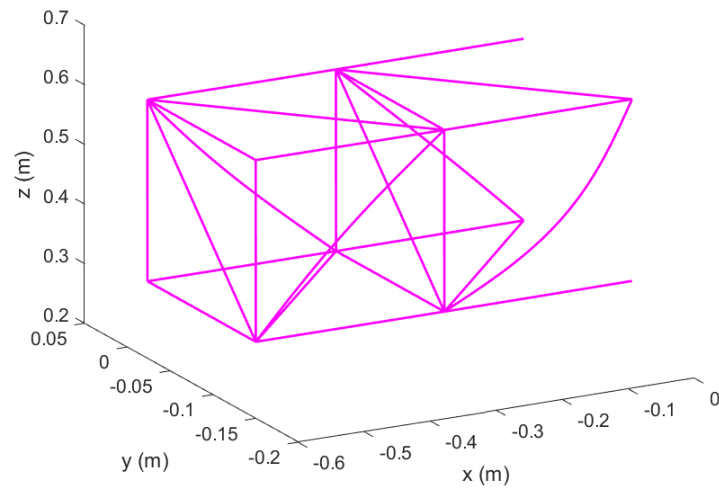


**Figure 37.** Mode 5 of Timoshenko beams in Topology 1 with hinged ends; spanwise expanded configuration.

**Table 8.** Change of Natural Frequencies,  $\omega(rad/s)$  of Timoshenko beam Analysis with Hinged ends in Topology 1, with spanwise expansion

Mode Number	Expansion (%)					
	0	2	5	10	15	20
Mode 1	1528.9	1483.4	1417.7	1315.2	1221.3	1135.4
Mode 2	1915.7	1876.4	1818.8	1726.2	1637.9	1553.9
Mode 3	1927.2	1888.1	1830.8	1738.7	1648.6	1562.9
Mode 4	1932.4	1892.4	1833.6	1738.9	1650.8	1567.3
Mode 5	1937.7	1897.9	1839.7	1746.5	1657.9	1573.6
Mode 6	1967.6	1927.2	1867.8	1772.5	1681.8	1595.7
Mode 7	1974.5	1933.9	1874.4	1778.7	1687.7	1601.2
Mode 8	1975.4	1934.8	1875.2	1779.6	1688.5	1602
Mode 9	2462.6	2392	2291.7	2137.8	1998.4	1871.2
Mode 10	2862.4	2774	2647.2	2450.6	2271	2106.7

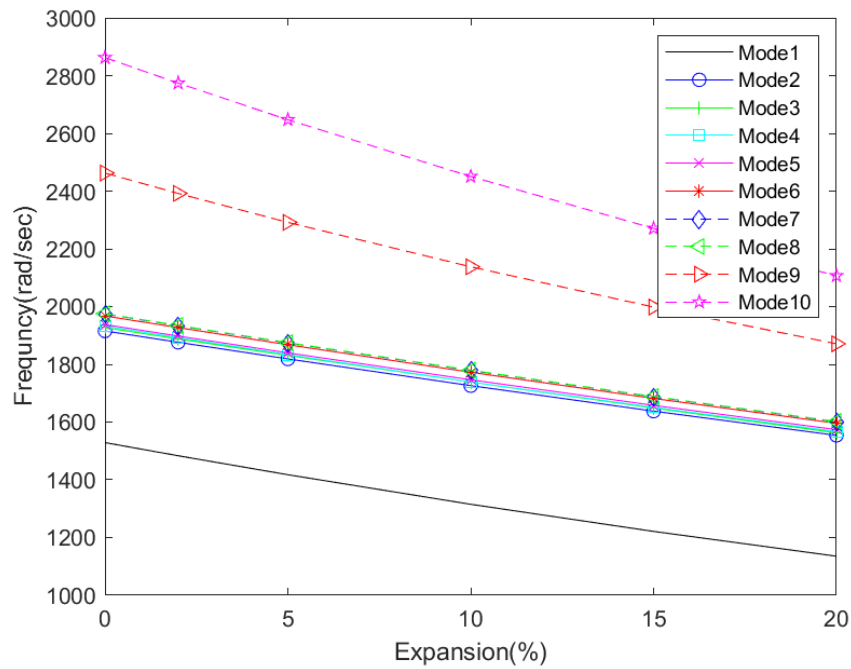


Figure 38. Changes in natural frequencies of Timoshenko beams with spanwise expansion.

4.5. Effect of Topology

All the analyses presented above were conducted on one topological configuration of the module (Topology 1). In this section, the modal analysis is conducted on a Topology 2 for the un-morphed configuration, shown in Figure 4 and represented here by a simplified line diagram in Figure 39. The first ten natural frequencies of Topology 2 are given in Table 9 for the same material and mechanical properties as those used in Topology 1. By comparing with Table 6, it is clear that this configuration of beam arrangement exhibit natural frequencies very close to those of Topology 1. Mode shapes are shown in Figures 40–44. It is clear here that vertical bending is small compared to the horizontal plane bending as in the case of Topology 1. However, it is observed that the second mode in fact represents twisting-bending coupling along with internal beam flexing. This coupling was not evident in Topology 1. However, the higher modes exhibit internal beam flexing as was also observed in Topology 1.

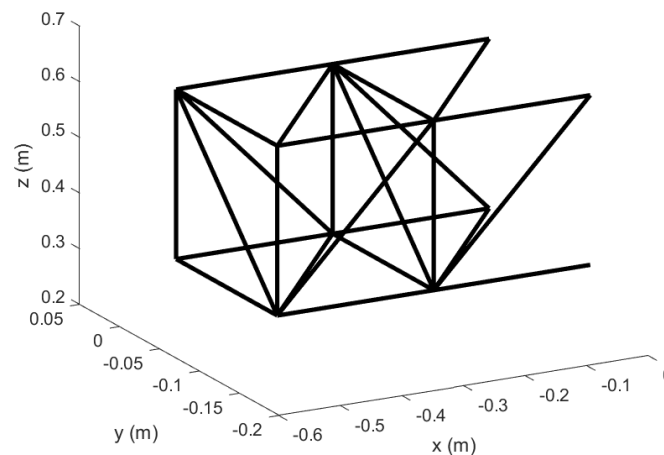
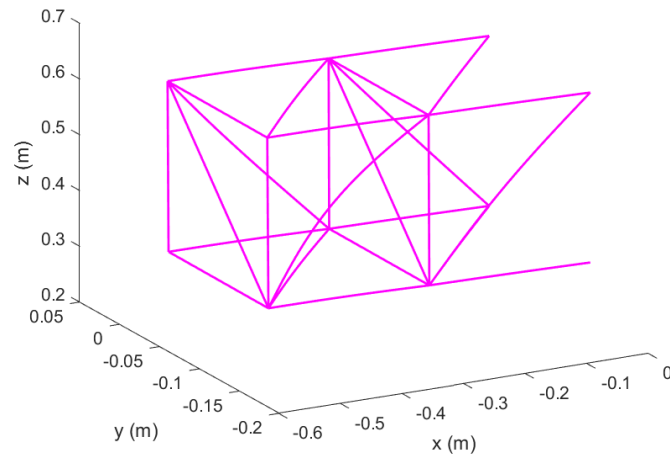
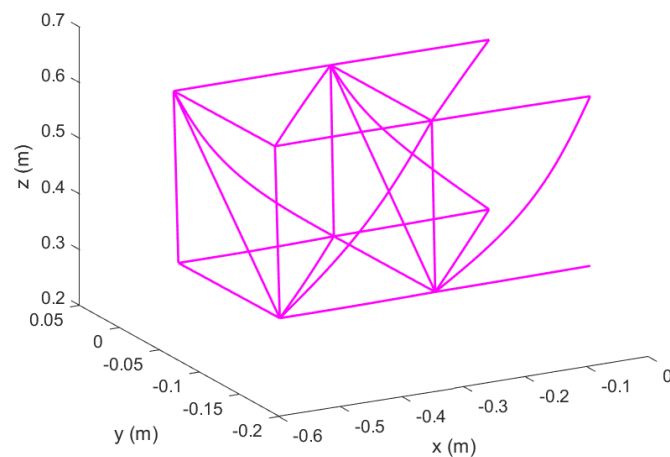
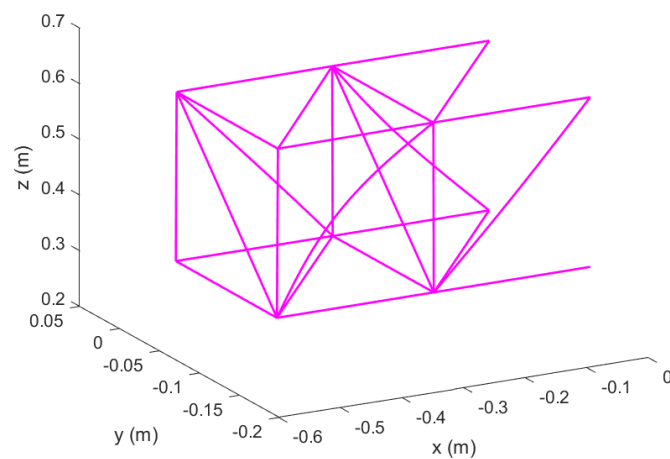
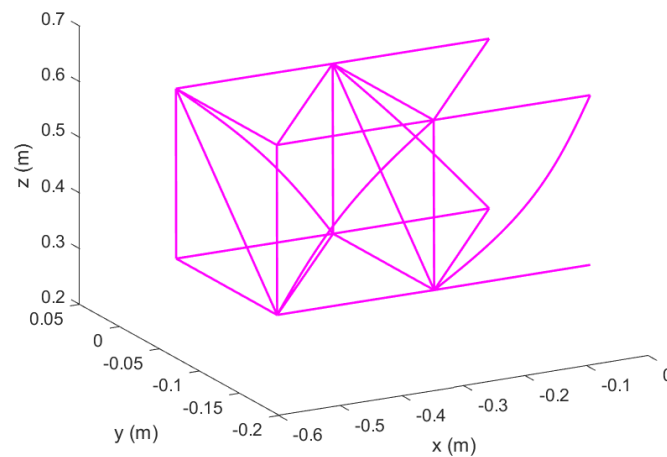


Figure 39. Un-morphed wing in Topology 2 with hinged ends; original configuration.

**Table 9.** Natural Frequencies,  $\omega$ (rad/s) of Timoshenko beam Analysis with Hinged ends in Topology 2, original configuration.

Mode	1	2	3	4	5	6	7	8	9	10
FEM	1547.3	1892.4	1923	1928.4	1937.8	1964.7	1974.5	1975.2	2480.1	2703.4

**Figure 40.** Mode 1 of Timoshenko beams in Topology 2 with hinged ends; original configuration.**Figure 41.** Mode 2 of Timoshenko beams in Topology 2 with hinged ends; original configuration.**Figure 42.** Mode 3 of Timoshenko beams in Topology 2 with hinged ends; original configuration.



**Figure 43.** Mode 4 of Timoshenko beams in Topology 2 with hinged ends; original configuration.

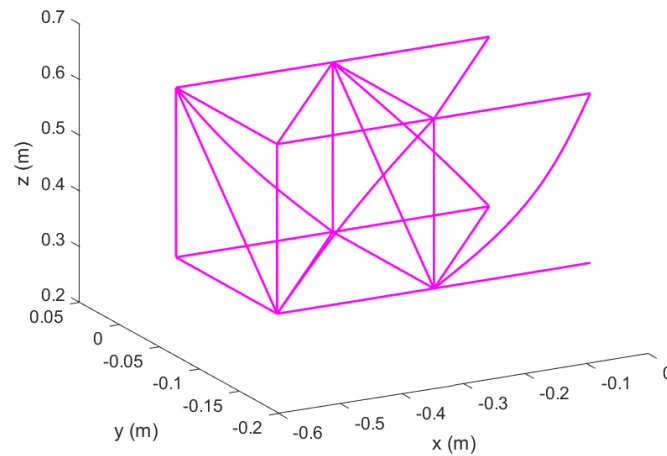


**Figure 44.** Mode 5 of Timoshenko beams in Topology 2 with hinged ends; original configuration.

## 5. Conclusions

Morphing wing aircraft have been reported to offer a high lift-to-drag ratio, a high performance in varying flight conditions, and enhancement in maneuverability and flight envelope. Notwithstanding these prospects, a cost is associated with it. Therefore, an optimum solution is sought for the conflicting outcomes. To this end, a consummate study of dynamic characteristics of the morphing wing must be conducted and comprehended. In this work, a special reconfigurable modular morphing wing design, developed in-house at Toronto Metropolitan University (formerly Ryerson University), has been studied. This modular design consists of a number of structural members connected through hinge joints. It is shown here that structural members/elements undergo bending, thereby truss element analysis is evidently a non-conservative approach. The effect of spanwise extension reported here exhibits a reduction in the natural frequencies of the system. It was also shown that the presented topology leads to unsymmetrical bending; vertical bending (flapping) is considerably high in amplitude compared to in-plane bending (lead-lag). Based on the two topological configurations studied here, it can be deduced that topology does not offer any considerable effect on the natural frequencies and mode shapes of the system. It can be concluded that the representation of a wing by one single beam or plate structural member does not provide the full dynamic characteristics of a wing. It is also deduced that, before deciding the number of modes to be included for a dynamic or aeroelastic analysis, more than ten modes and mode shapes must be computed and included to provide reliable aeroelastic characteristics of the wing.

**Author Contributions:** This paper presents the results of recent research conducted by the first author (F.M.) under the co-supervision of the second (S.M.H.) and third (H.A.) authors. All authors have read and agreed to the published version of the manuscript.

**Funding:** This research was partially supported by a Discovery Grant from the Natural Sciences and Engineering Research Council of Canada (NSERC), RGPIN-2017-06868.

**Institutional Review Board Statement:** Not applicable.

**Informed Consent Statement:** Not applicable.

**Data Availability Statement:** All data generated or analyzed during this study are included within the article.

**Acknowledgments:** Support provided by the National Sciences and Engineering Research Council of Canada (NSERC), the Ontario Graduate Scholarship (OGS) program, the Queen Elizabeth II Graduate Scholarship in Science and Technology (QEII-GSST), and Toronto Metropolitan University (formerly Ryerson University), is highly acknowledged.

**Conflicts of Interest:** The authors declare that there are no conflicts of interest regarding the publication of this paper.

## Abbreviations

The following abbreviations are used in this manuscript:

DOF	Degrees of Freedom
DSM	Dynamic Stiffness Matrix
FEA	Finite Element Analysis
FEM	Finite Element Methodology

## References

1. Barbarino, S.; Bilgen, O.; Ajaj, R.; Friswell, M.; Inman, D. A review of morphing aircraft. *J. Intell. Mater. Syst. Struct.* **2011**, *22*, 823–877. [\[CrossRef\]](#)
2. Previtali, F.; Arrieta, A.F.; Ermanni, P. Performance of a three-dimensional morphing wing and comparison with a conventional wing. *AIAA J.* **2014**, *52*, 2101–2113. [\[CrossRef\]](#)
3. Finistauri, A.D. Conceptual Design of a Modular Morphing Wing. Ph.D. Thesis, Department of Aerospace Engineering, Ryerson University Toronto, ON, Canada, 2013.
4. Ramrakhani, D.S.; Lesieutre, G.A.; Frecker, M.; Bharti., S. Aircraft structural morphing using tendon-actuated compliant cellular trusses. *J. Aircr.* **2005**, *42*, 1615–1620. [\[CrossRef\]](#)
5. Moosavian, A. Variable Geometry Wing-Box: Toward a Robotic Morphing Wing. Ph.D. Thesis, Department of Aerospace Engineering, Ryerson University, Toronto, ON, Canada, 2014.
6. Moosavian, A.; Xi, F.; Hashemi, S.M. Design and Motion control of fully variable morphing wings. *J. Aircr.* **2013**, *50*, 253–264. [\[CrossRef\]](#)
7. Mahmood, F. Transient Response of Varying Thickness Timoshenko beam under Point Load. Master's Thesis, Department of Mechanical Engineering, King Fahd University of Petroleum and Minerals, Dhahran, Saudi Arabia, 1999.
8. Logan, D.L. *A First Course in the Finite Element Method*, 5th ed.; Cengage Learning: Stamford, CT, USA.
9. Davis, R.; Henshell, R.; Warburton, G. A Timoshenko beam element. *J. Sound Vib.* **1972**, *22*, 475–487. [\[CrossRef\]](#)
10. Wittrick, W.; Williams, F. A general algorithm for computing natural frequencies of elastic structures. *Quart. J. Mech. Appl. Math.* **1971**, *24*, 263–284. [\[CrossRef\]](#)
11. Williams, F.; Wittrick, W. An automatic computational procedure for calculating natural frequencies of skeletal structures. *Int. J. Mech. Sci.* **1970**, *12*, 781–791. [\[CrossRef\]](#)
12. Banerjee, J.; Ananthapuvirajah, A. An exact dynamic stiffness matrix for a beam incorporating Rayleigh–love and Timoshenko theories. *Int. J. Mech. Sci.* **2019**, *150*, 337–347. [\[CrossRef\]](#)
13. Yu, C.P.; Roesset, J.M. Dynamic stiffness matrices for linear members with distributed mass. *Tamkang J. Sci. Eng.* **2001**, *4*, 253–264.
14. Malik, A. Free Vibration of Rods, Beams and Frames. Master's Thesis, National Institute of Technology Rourkela, Rourkela, India, 2013.